Research article

Applicability of RANS models and pressure drop in edge subchannels for 19-pin wire-wrapped fuel bundle channel in CiADS

Dajun Fan [a,b,c,1], Rongjie Li [a,b,1], Ruoxiang Qiu [d], Minghan He [a,b], Jiatai Liu [a,b], Yanze Tang [a,b,c], Lu Zhang [a,b], Dawei Cui [d], Liming Zhu [a,b], Long Gu [a,b,e,*], Yue Li [a,**]

[a] Institute of Modern Physics, Chinese Academy of Sciences, Lanzhou, 730000, China
[b] School of Nuclear Science and Technology, University of Chinese Academy of Sciences, Beijing, 100049, China
[c] Advanced Energy Science and Technology Guangdong Laboratory, Huizhou, 516003, China
[d] China Nuclear Power Technology Research Institute Co., Ltd., Shenzhen, 518000, China
[e] School of Nuclear Science and Technology, Lanzhou University, Lanzhou, 730000, China

A R T I C L E   I N F O

A B S T R A C T

The accelerator-driven subcritical system has a strong transmutation ability and high inherent safety, and it is internationally recognized as the most promising long-life nuclear waste disposal device. This study involves the construction of a Visual Hydraulic ExperimentaL Platform (VHELP) for the purpose of evaluating the applicability of Reynolds-averaged Navier–Stokes (RANS) models and analyzing the pressure distribution within the fuel bundle channel of China initiative accelerator-driven system (CiADS). Measurements of thirty differential pressures in edge subchannels within a 19-pin wire-wrapped fuel bundle channel were obtained under different conditions using deionized water. The pressure distribution in the fuel bundle channel at Reynolds numbers of 5000, 7500, 10,000, 12,500, and 15,000 was simulated using Fluent. The results show that RANS models obtained accurate results, and the shear stress transport k-ω model provided the most accurate prediction of the pressure distribution. The difference between the results of the Shear stress transport (SST) k-ω model and experimental data was the smallest, and the maximum difference was ±5.57%. Moreover, the error between the experimental data and numerical results of the axial differential pressure was smaller than that of the transverse differential pressure. The pressure periodicity in axial and transverse directions (one pitch) and a relatively three-dimensional pressure measurements were studied. The static pressure fluctuated and decreased periodically as the z-axis coordinate increased. These results can facilitate research on the cross-flow characteristics of liquid metal-cooled fast reactors.

1. Introduction

The safe disposal of spent fuel produced by nuclear power plants, particularly long-lived and highly radioactive waste, is one of the

challenges for the sustainable development of nuclear power. Lead-cooled fast reactors (LFRs) employ lead or lead-bismuth eutectic (LBE) as the coolant and operate at atmospheric pressure. LBE exhibits several benefits in terms of its good neutron economy, high thermal conductivity, high boiling point, and strong chemical inertness. Consequently, an LFR was chosen as the subcritical reactor in the China initiative accelerator-driven system (CiADS). It consists of a superconducting proton linear accelerator, a high-power LBE spallation target, a sub-critical reactor, and multiple experimental terminals [1–3]. The total thermal power of the accelerator beam and reactor is less than or equal to 10 MW. The construction of CiADS will be completed by the end of 2027, and it will be the first megawatt-accelerator-driven transmutation system in the world. The fuel assembly of the reactor in CiADS consists of 162 fuel pins and seven guide tubes arranged in a regular triangle. The enrichment of the UO_2 ceramic fuel is 19.75 wt%.

Wire-wrap spacers are typically used as positioning components in the fuel assembly in liquid metal-cooled fast reactors. They serve multiple functions, including preserving fuel pin spacing, reducing fuel pin vibration, and boosting the convective heat transfer performance of working fluids. The flow characteristics in a fuel assembly significantly influence the security and economy of nuclear systems. However, it is difficult, dangerous, and expensive to perform experiments using LBE for the following reasons: (1) LBE exhibits corrosive properties towards structural materials and possesses an opaque nature; (2) LBE operates at high temperatures, and LBE vapor is harmful to humans; and (3) LBE, experimental equipment, and protective appliances are expensive [4,5]. However, if the Reynolds similarity criterion is met, it is possible to analyze the flow characteristics of LBE through tests with alternative working fluids. This can be achieved by designing an appropriate test section and selecting an alternative working fluid [6–9]. In previous decades, researchers have experimentally and numerically investigated the hydraulic characteristics in a wire-wrapped fuel bundle channel on the basis of dimensional analysis and similarity theory.

(1) Experimental research: Vaghetto et al. [10] used p-Cymene as the working fluid (medium) and investigated the pressure drop in a 61-pin wire-wrapped fuel assembly with a lead pitch of 476 mm. They found that the detailed Cheng and Todreas correlation [11] provided the most accurate prediction of pressure drop. Liang et al. [12] measured the pressure drop in different sub-channels in a 37-pin wire-wrapped fuel assembly using deionized water, with a pitch-to-rod diameter ratio (P/D) = 1.09 and lead-pitch-to-rod diameter ratio (H/D) = 9.55. The largest and smallest friction factors in edge and corner subchannels were obtained, respectively. Padmakumar et al. [13] measured the pressure distribution in a 217-pin wire-wrapped fuel assembly using water as the working fluid with a lead pitch of 200 mm. They found that the experimental data deviated from the results obtained using friction factor formulas and predicted no sodium boiling risk. Jeong et al. [14] studied the pressure loss in a U-pattern wire-wrap spacer fuel assembly using water. The loss coefficient of this spacer was similar to that of a conventional wire-wrap spacer at low Reynolds numbers but larger than that of the conventional spacer at high Reynolds numbers. Childs et al. [15] conducted transverse pressure difference measurement on a fuel assembly model with 61 pins and wire-wrapped spacers across a range of Reynolds numbers spanning from 3000 to 18,000. Based on the experimental findings, when the wire-wrap spacer was aligned with the corner of two neighboring faces in the hexagonal duct, the experimental results revealed the coexistence of maximum and minimum pressure at different faces simultaneously. Furthermore, the transverse pressure distribution was found to be influenced by the flow regime. Menezes et al. [16] conducted experiments to measure the local pressure drops in different subchannels within a 61-pin wire-wrapped rod bundle at Reynolds number from 190 to 22,000. The results indicated that the interior subchannels contributed equally to the average friction factor, while the edge subchannel showed the lowest value. Their study provided experimental data of pressure drop in interior subchannels and a more comprehensive understanding of the hydraulic phenomenon in the wire-wrapped fuel assembly. Nguyen et al. [17] conducted Particle Image Velocimetry (PIV) experiments on a 5 × 5 bundle with a spacer grid and mixing vanes under the Reynolds number of 14,000. The results showed that vortex shedding frequencies contributed to the coherent functions' peaks, which was the first experimental evidence of anisotropy flow. This provides an explanation for the RANS turbulent models' poor performance that employ the linear eddy viscosity approach. Goth et al. [18] investigated the flow field distribution within a 61-pin wire-wrapped fuel assembly with PIV when the Reynolds number was 19,000. The experimental data allowed for the determination of the average velocity, root-mean-square (RMS) fluctuating velocity and the Reynolds stress of the flow field.

(2) Numerical research: Kim et al. [19] used STAR-CCM + to calculate the flow characteristics in a 37-pin fuel assembly featuring a pin-to-rod diameter ratio of 1.13, with deionized water utilized as the working fluid. The results derived from the k-ε model displayed excellent concurrence with experimental data. Jeong et al. [20] used CFX to examine the flow characteristics in a fuel assembly with 127 pins and wire-wrapped spacers, which possessed a pitch measuring 293.9 mm. The ratio of axial flow to tangential flow in edge and corner subchannels was larger than that in the internal subchannels. Liu et al. [21] used Fluent to study the impact of four circular wire-wrap spacers and four trapezoidal wire-wrap spacers on the pressure distribution within a 19-pin fuel assembly possessing a pitch measuring 215 mm. In their study, water was implemented as the working fluid. The frictional pressure drops induced by the circular wire-wrap spacers were smaller than those induced by the trapezoidal wire-wrap spacers. Merzari et al. [22] compared the results obtained using Reynolds-averaged Navier–Stokes (RANS) models and the large–eddy simulation method. The RANS models exhibited high precision. Dovizio et al. [23,24] assessed four different RANS models, such as linear Shear stress transport (SST) k-ω, realizable k-ε, k-ω SST cubic, and Reynolds Stress Model (RSM)-EB Model, through a Direct Numerical Simulation (DNS) database, Large Eddy Simulation (LES) database, and experimental measurements. The overall deviations of RANS models relative to the q-DNS were under 10%. They are able to provide reasonably good results for wire-wrapped bundles. Bovati et al. [25] employed RANS models and LES methods to study the pressure differences in the transverse direction in a 61-pin wire-wrapped fuel assembly. The CFD results were validated by experimental results and the predictions of Upgraded Chen and Todreas Detailed (UCTD) correlation. The results indicated that *k-ω* models predicted friction factor better than *k-ε* models but no obvious differences were found in the transverse pressure

drop. The SST k-ω cubic model fitted well for both transition and fully turbulent flow regimes. Bovati et al. [26] applied three turbulent models for the accident of local blockage in a 61-pin wire-wrapped hexagonal duct model, and compared their results with experimental data in the previous work [27]. Their comparison results recommended employing Reynolds Stress Model (RSM) and Realizable k-ε to the turbulent regime, and SST k-ω to the transition regime.

This study aims to further evaluate the application of RANS models and study the pressure drop in edge subchannels. For this purpose, the axial and transverse differential pressures in the edge subchannels [28,29] in a 19-pin wire-wrapped fuel assembly model were investigated through experiments and simulations. Furthermore, this study analyzes the cross-flow characteristics in the fuel bundle channel. These results can improve the understanding of pressure distribution in a wire-wrapped fuel bundle in the CiADS.

2. Experimental method

As shown in Fig. 1, a Visual Hydraulic ExperimentaL Platform (VHELP) was designed and built [30,31]. It consisted of a primary loop and a secondary loop. The secondary loop regulated the temperature of the working fluid in the primary loop through a heat exchanger and a water chiller. To ensure optimal performance, deionized water was selected as the working fluid and maintained at an operating temperature of 29.0 $\pm$ 0.5 °C.

2.1. Test section

The test section was a 19-pin wire-wrapped fuel assembly model, which was fabricated from polymethyl methacrylate and stainless steel. The diameters of the fuel rod and wire-wrap spacer were 12.903 mm and 1.953 mm, respectively, which were the same as those utilized in the reactor of the CiADS. The lead pitch of the wire-wrap spacer was 144.000 mm, and there were seven pitches. The wire-wrap spacer rotated in the clockwise direction. The inner side length of the hexagonal duct was 40.200 mm. The geometric precision of wire-wrap spacers was an essential factor in this experiment. The wire-wrap spacers were wrapped around the fuel pins with high precision and efficiency using a gear synchronous positioning device. Fig. 2(a) and (b) show the first pitch of pins and the bottom plugs of three-dimensional model and picture, respectively. Here, the notation SP denotes the starting point of wire-wrap spacers, while 1R signifies the first row. 316L stainless steel was used to manufacture bottom plugs, which can facilitate the fuel pin assembly and enhance mechanical strength.

The test section was installed vertically, with deionized water flowing from the bottom to the top. A DN50 flange utilized as the inlet, while the outlet consisted of two symmetrical DN32 flanges. Fig. 3 shows the layout of 30 differential pressure transducers. The axial direction of the fuel assembly was divided into four cross-sections, each with different z-axis coordinates. Six pressure taps were
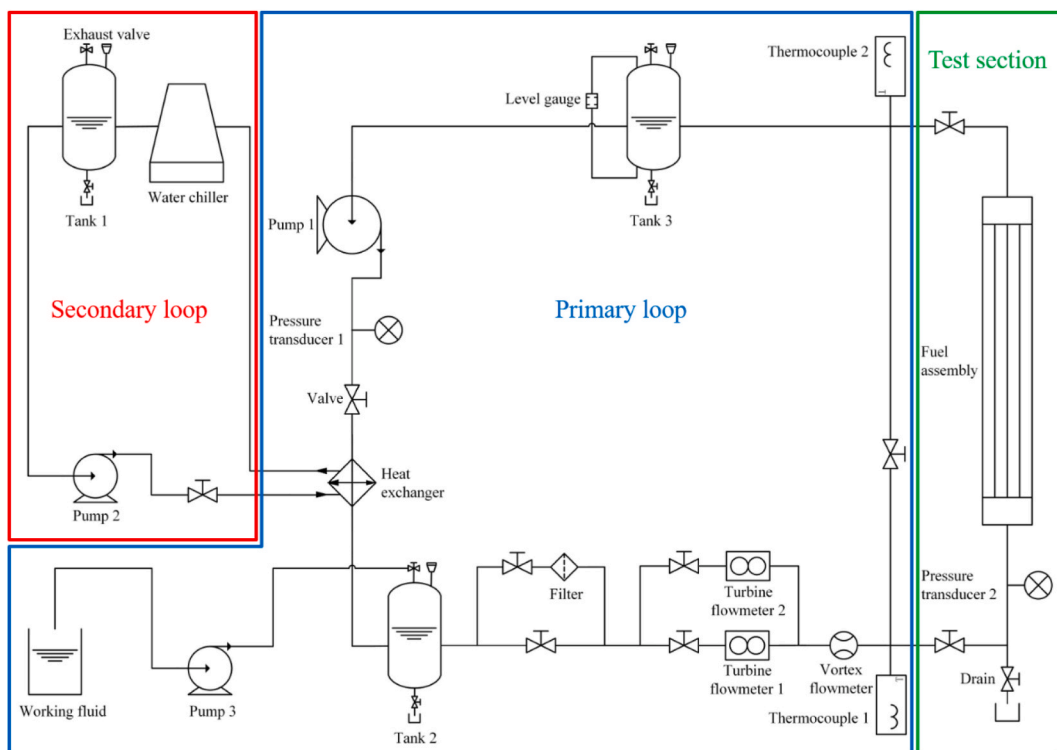

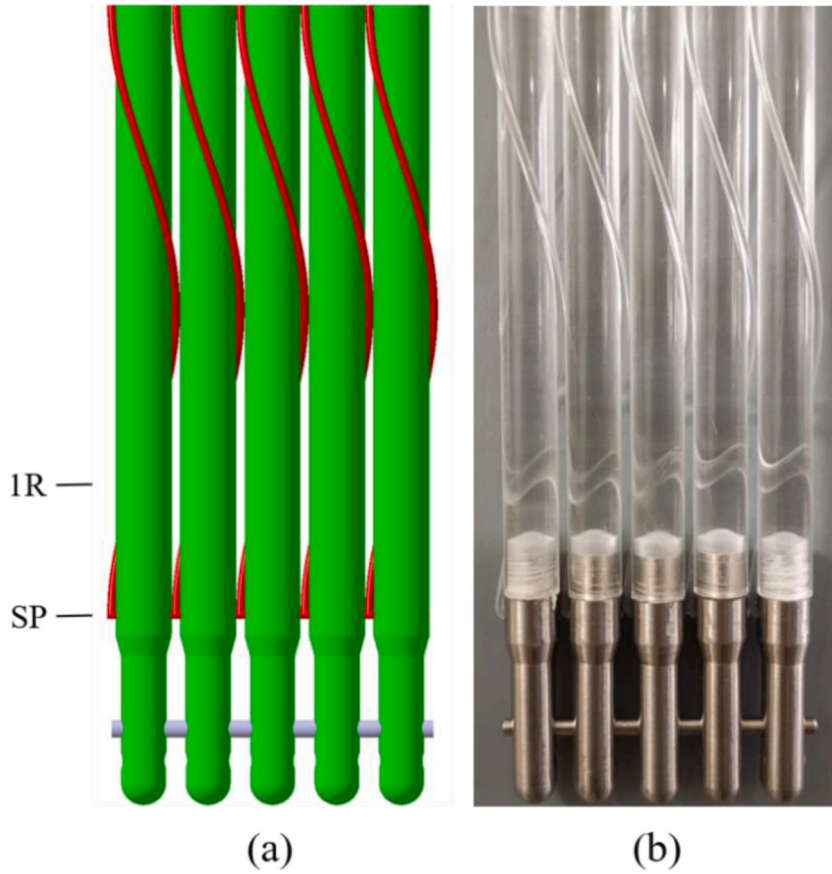**Fig. 1.** Flow chart of Visual Hydraulic ExperimentaL Platform (VHELP).

Fig. 2. First pitch of fuel pins: (a) three-dimensional model and (b) picture.

positioned at the middle point of each side of the hexagonal duct. The lead pitch H was used as a reference to express the distances between 1R and second row (2R), 2R and third row (3R), and 3R and fourth row (4R), which were measured as 432.0 mm (3.0H), 288.0 mm (2.0H), and 216.0 mm (1.5H), respectively.

Three-way pipes and four-way pipes were used to measure 18 axial differential pressures and 12 transverse differential pressures in a Reynolds number range of 3750–16250. Because the movement of air bubbles strongly affected the measurement accuracy, two three-way needle valves were connected to each side of differential pressure transducers for removing the air bubbles in the pressure pipe and controlling the on–off operation. Moreover, Fig. 4 illustrates the presence of a multi-layer screen filter plug arranged in the bottom nozzle, which was used to guarantee uniform flow rates.

The Reynolds number, Re, was calculated according to equation (1).

$$\mathrm{Re} = \frac{\rho V De}{\mu} \tag{1}$$

where ρ is the density, V is the velocity, De is the bundle hydraulic diameter, and μ is the viscosity of the working fluid. The wire-wrapped spacer geometry has been considered when calculating the hydraulic diameter using equation (2).

$$De = 4\frac{A}{L_f} = 4\frac{6a^2\frac{\sqrt{3}}{4} - \frac{N_r\pi\left(D_r^2 + D_w^2\right)}{4}}{6a + N_r\pi(D_r + D_w)} = \frac{6\sqrt{3}a^2 - N_r\pi\left(D_r^2 + D_w^2\right)}{6a + N_r\pi(D_r + D_w)} \tag{2}$$

where a is the side of the duct, mm, Nr is the number of the pins, Dr and Dw is the diameter of the rod and wire-wrapped spacers, mm, respectively. And the hydraulic diameter of this fuel assembly model is 6.016 mm.

Fig. 5 shows the schematic of the arrangement of the 24 pressure taps. Fig. 5(a) shows the distribution of the four cross sections. Fig. 5(b) shows the cross section at starting point (SP) of the wire-wrap spacers. Fig. 5(c) shows the cross sections at 1R, 2R, and 3R. Fig. 5(d) shows the cross section at 4R. The measurement zones were as follows: The pressure at the pressure tap in the back is subtracted from the pressure at the pressure tap in the front. Pa and Pt represent axial and transverse differential pressures, respectively. For example, Pa (31–41) represents the pressure at pressure tap 31 minus that at pressure tap 41. If the value is positive, the pressure at pressure tap 31 is higher than that at pressure tap 41. Otherwise, the pressure at pressure tap 41 is higher than that at pressure
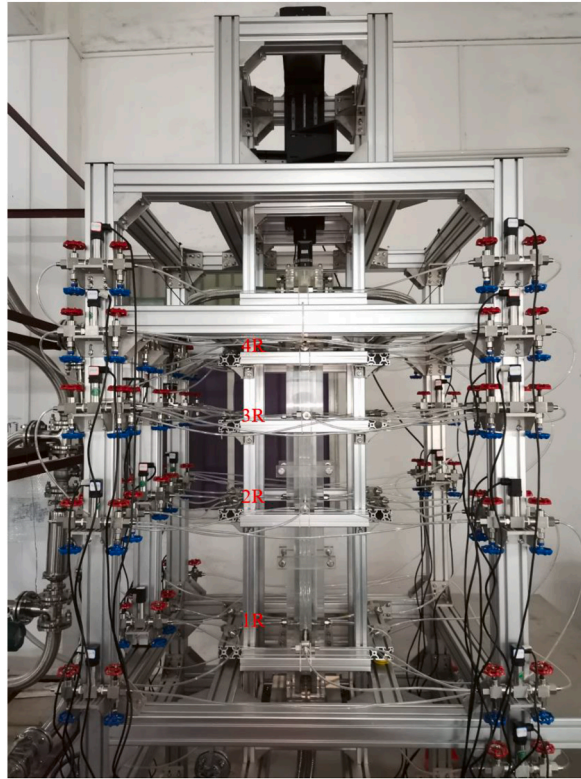
Fig. 3. Photograph of the pressure transducer arrangements.

Fig. 4. The multi-layer screen filter plug in the bottom nozzle.

tap 31.

2.2. Test loop

Two turbine flowmeters with ranges of 1.5–15 m^3/h ($\pm$0.5%) and 4.0–40 m^3/h ($\pm$0.5%), were connected in parallel to cover a wider range of working conditions and improve the measurement accuracy. Additionally, a vortex flowmeter with a measuring range of 5.0–50 m^3/h ($\pm$1.0%) was installed in the loop, as a backup measurement device. These two types of flowmeters were used for mutual verification and provide redundancy in case of any failure in one of the flowmeters. Twelve differential pressure transducers with a range of $\pm$10 kPa ($\pm$0.15%) and 18 differential pressure transducers with a range of $\pm$20 kPa ($\pm$0.15%) were employed to measure the differential pressures in the edge subchannels. Thermocouples were positioned at the inlet and outlet of the test section to measure the temperature change simultaneously. The measurement and control system compiled using LabVIEW was used to realize the following functions: (1) start and stop of the platform; (2) adjustment of the pump frequency; and (3) monitoring and saving the data of the flowmeters, pressure transducers, and thermocouples.
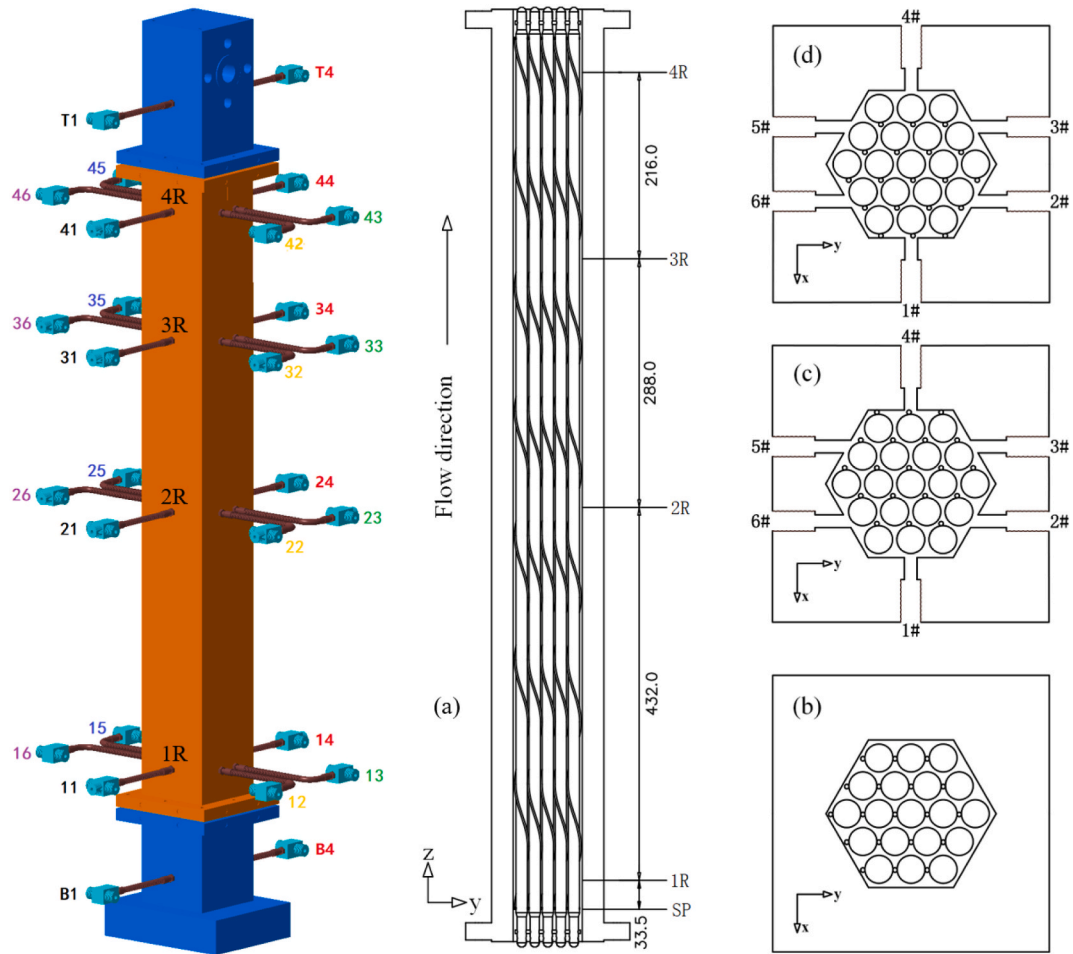
Fig. 5. Arrangement of pressure taps (unit: mm): (a) distribution of the four cross sections; (b) cross section at starting point (SP) of the wire-wrap spacers; (c) cross sections at 1R, 2R, and 3R; (d) cross section at 4R

3. Numerical method

Experimental measurements can only provide limited and macroscopic pressure distribution data, whereas computational fluid dynamics (CFD) calculations can provide considerably detailed microscopic flow characteristics. In this study, Fluent was employed to simulate the flow characteristics in the fuel bundle channel.
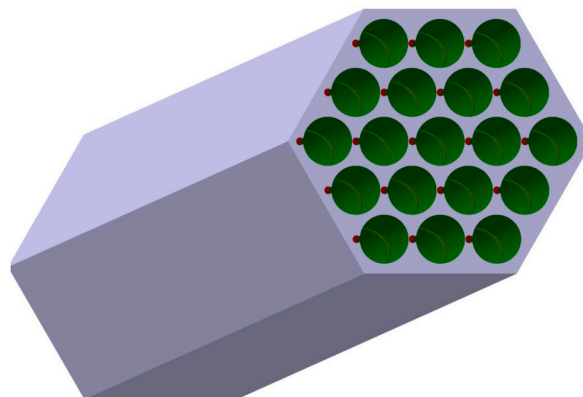
Fig. 6. Three-dimensional model of the flow channel.

3.1. Three-dimensional modeling and grid generation

Roelofs et al. [32] reviewed the challenges associated with studying the flow characteristics in a wire-wrapped fuel assembly and emphasized the crucial role of grid generation. In this work, CATIA was used to create the three-dimensional model of the flow channel (Fig. 6). The line contact and shape edge are significant challenges in grid generation. Thus, a wire-wrap spacer was indented in the direction of its fuel rod, with a gap of 0.1 mm between the wire-wrap spacer and the neighboring fuel rod. A fillet radius of 0.25 mm was employed to reduce the difficulty of grid generation. The geometric simplification has been shown to have a negligible effect on the flow characteristics in a wire-wrapped fuel bundle channel in previous studies [22,33–35]. STAR-CCM+ was employed to generate a polyhedral mesher and prism layer. Compared to a tetrahedral mesh, a polyhedral mesh has fewer cells and a faster convergence speed. Fig. 7 shows the grid distribution at the inlet.

3.2. Iterative calculation

The flow characteristics in the 19-pin fuel bundle channel were obtained at Reynolds numbers of 5000, 7500, 10,000, 12,500, and 15,000. The velocity inlet and pressure outlet boundary conditions were employed. The SST k-ω [21,22,36], standard k-ω, and realizable k-ε turbulence models and the Semi-Implicit Method for Pressure Linked Equations (SIMPLE) numerical algorithm were selected. The cross section at the starting point (SP) was considered as the origin of the z-axis. Mesh sensitivity was examined using five meshes with different basic sizes—2.1 mm (30,851,367 cells), 1.9 mm (34,299,137 cells), 1.7 mm (40,206,023 cells), 1.5 mm (47,448,443 cells), and 1.3 mm (55,873,840 cells). There were four boundary layers on the wall, fuel rods, and wire-wrap spacers, with a total height of 0.025 mm on each side. The relationships between the static pressure and z-axis coordinate on column 1 at a Reynolds number of 15,000 (in turbulent region) are shown in Fig. 8. Column 1 refers to the line parallel to the z-axis that passes through pressure measurement point 1. There was no significant difference between the static pressures on column 1 obtained using the five meshes. Thus, the calculation results were independent of the mesh size. In addition, the axial static pressure fluctuated and decreased periodically as the z-axis coordinate increased [37]. Mesh 4 was selected on the basis of the calculation time and accuracy.

4. Results and discussion

The evaluation of the friction factor models: Rehme [38], Cheng and Todreas [39], Novendstern [40], Engel [41], and zhukov [42], using experimental data has been done, and the transition from transitional to turbulent flow regimes has been studied in the previous study [32]. Thus, we focus on the applicability of RANS models and pressure drop in edge subchannels in this section.

The static pressures at different pressure taps were exported in Fluent. Then, the pressure at one pressure tap was subtracted from the pressure at the next pressure tap to obtain the differential pressure between these pressure taps. A comparison between the experimental data and numerical results of different RANS models of the axial differential pressure is shown in Fig. 9. R denotes a row, and Pa (1R–2R) denotes the average of six differential pressure measurements between rows 1 and 2, namely, Pa (11–21), Pa (12–22), Pa (13–23), Pa (14–24), Pa (15–25), and Pa (16–26). Exp and Num denotes the experimental data and numerical result, respectively. The CFD results based on the RANS models could effectively capture the pressure drop characteristics in the wire-wrapped fuel bundle channel. The difference between the results of the SST k-ω model and experimental data was the smallest, and the maximum difference was ±5.57%. The SST k-ω model slightly over-predicted the turbulence levels compared with the experimental data. This was probably because there are larger regions with smaller velocities [43,44]. However, this trend was far less pronounced than in the other turbulence models. Therefore, the results obtained using the SST k-ω model were considered for further analysis.

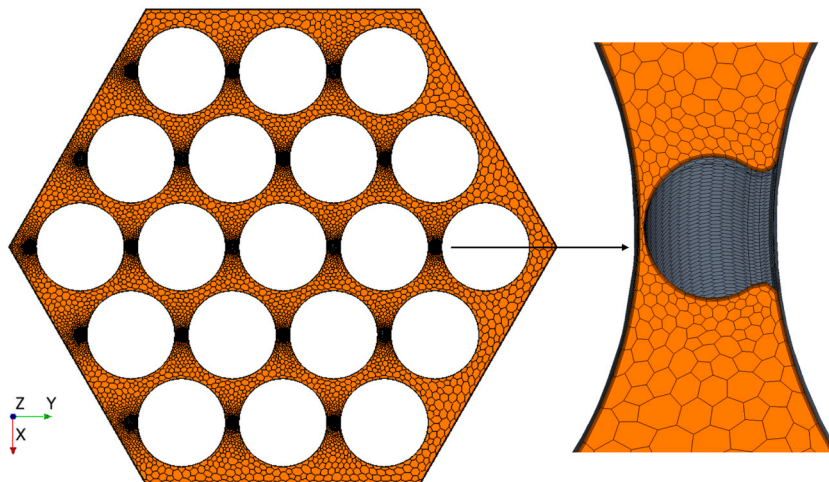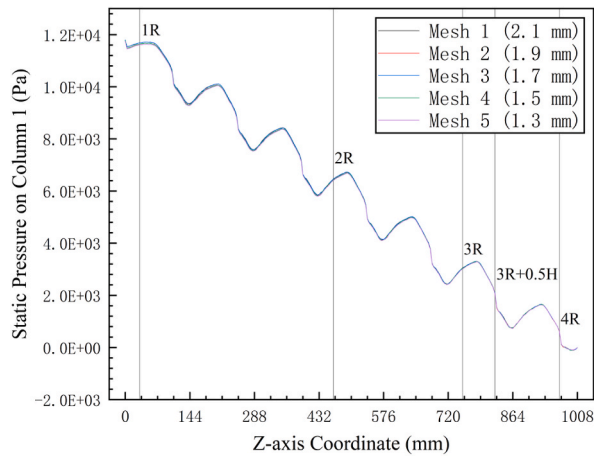**Fig. 7.** Grid distribution of the fuel assembly.
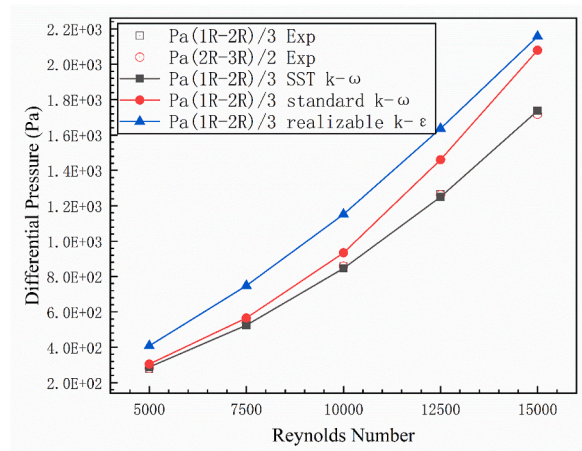
Fig. 8. Mesh sensitivity study.

Fig. 9. Comparison between the experimental data and numerical results of different RANS models of axial differential pressure.
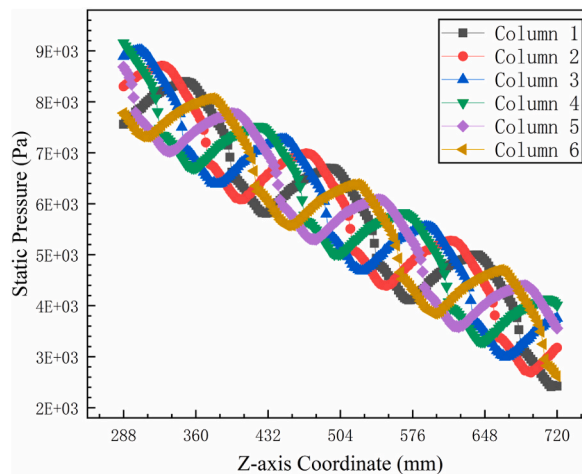

Fig. 10. Variation in static pressures with the z-axis coordinate on different columns between 2.0H and 5.0H when the Reynolds number was 15,000.

Fig. 10 shows the variation in the static pressure with the z-axis coordinate on different columns between 2.0H and 5.0H at a Reynolds number of 15,000. The pressure change trends for the other five columns were similar, except for the phase difference (1/6 H) caused by the starting angle of the wire-wrap spacers around the pressure taps. The maximum difference between the experimental data Pa (1R–2R)/3 and Pa (2R–3R)/2 in Fig. 9 was ±2.18%. Therefore, Figs. 9 and 10 show that the fluctuation period of the static pressures in the axial direction was 1.0 pitch (H). The axial differential pressure between two cross sections at 1.0H was constant at a certain Reynolds number.

Fig. 11 shows the variation in the transverse differential pressure with the z-axis coordinate between 2.0H and 5.0H. Pt (1#- 4#) denotes the static pressure at the point on column 4 subtracted from that on column 1. If the value is positive, the static pressure on column 1 is higher; otherwise, the static pressure on column 4 is higher. The transverse differential pressure between the two pressure taps in the 180° direction in the edge subchannels varied periodically with the z-axis coordinate. The variation was similar to the sine function, and the variation period was 1.0H. Except for the minor fluctuation close to the wire-wrapped spacers, the phase difference between two adjacent curves was 1/6 H. The ratio of the maximum transverse differential pressure (~1670 Pa) to the average axial pressure drop within 1.0H (~1756 Pa) was approximately 95%. This ratio varied with the z-axis coordinate of the pressure taps in the 180° direction.

Fig. 12 shows the pressure drops in 0.5H at different Reynolds numbers. The symbol ' denotes the differential pressures in 0.5H, which were obtained by subtracting the differential pressures in 1.5H from those in 1.0H. Exp and Num denote the experimental data and numerical results, respectively. The axial pressure difference increased with the Reynolds number; this agreed with the Darcy–Weisbach formula trend. As shown in Fig. 5(c) and (d), the flow path of deionized water along the wire-wrap spacers was similar in columns 2 and 3 and in columns 5 and 6 within 0.5H. Thus, the curves for these columns were quite close. The maximum and minimum differential pressures were observed in column 2 (column 3) and column 5 (column 6), respectively. As the wire-wrap spacers rotated clockwise, the volume proportion of the wire-wrap spacers in the edge subchannels where the pressure taps were located between the cross sections at 3R and 4R decreased in the following order: column 2 (column 3), column 4, column 1, column 5 (column 6). The differential pressures in columns 5 and 6 were negative, which corresponded to the pressure distribution curve shown in Fig. 10.

It was challenging to accurately measure transverse differential pressure, particularly when the pressure taps were located close to the wire-wrap spacers. Figs. 13 and 14 show the comparison between the experimental data and numerical results of the transverse differential pressures at 1R and 4R under different conditions, respectively. The experimental data generally agreed with the numerical results, demonstrating the applicability of SST k-ω model again. The trend of the transverse differential pressure shown in Fig. 14 was opposite to that shown in Fig. 13, and the absolute values of the pressure were not the same. Because the axial static pressure change along the flow direction was non-linear, it was a non-standard sine function. The deviation between the experimental and numerical results of the transverse differential pressure was larger than that of the axial differential pressure. This was because the transverse differential pressure was smaller than the axial differential pressure and the pressure gradient close to the wire-wrap spacers was larger.

The CFD simulation results provide a preliminary reference for a test section design; additionally, they provide more detailed micro data that are difficult to obtain experimentally, as an extension of experimental measurements. This can improve the accuracy and efficiency of measurements, reduce measurement times, save manpower, capital, and computing resources. The CFD simulation results validated using experiments data can provide more detailed flow field information, particularly in the zones close to the wire-wrap spacers. Fig. 15 shows the pressure distribution contours on the four cross sections at a Reynolds number of 15,000. The wire-wrapping structure enhanced the mixing of the working fluid, the flow close to the wire-wrap spacers changed significantly. The pressure distributions shown in Fig. 15(a)–(c) were almost the same, and the pressure distribution in Fig. 15(d) was opposite to that in the first three figures, demonstrating that the periodicity was 1.0H. The black arrows in the contours indicate the wire-wrap spacers' rotation direction.

Fig. 16 shows the pressure contours at different cross sections from 3.0H to 3.0 and 5/6 H at intervals of 1/6 H. Fig. 16(a)–(f) show the pressure contours at 3.0H, 3.0 and 1/6 H, 3.0 and 1/3 H, 3.0 and 1/2 H, 3.0 and 2/3 H, and 3.0 and 5/6 H, respectively. When the axial height increased by 1/6 H, the pressure distribution contours rotated clockwise by 60° and the pressure values fluctuated and decreased. Therefore, the pressure periodicity in the transverse direction was 1.0H. There were apparent high-pressure and low-pressure areas in the transverse direction and strong pressure gradients close to the wire-wrap spacers. The high-pressure area appears at about 90° forward of the wire-wrap spacers's rotation direction. In the first half-pitch, deionized water experienced strong friction resistance on the right side of the wire-wrap spacers. In contrast, in the second half-pitch, deionized water experienced strong resistance on the left side of the wire-wrap spacers when it flowed from the bottom to the top.

5. Conclusion

In this study, a VHELP was constructed to examine the pressure distribution in a 19-pin wire-wrapped fuel bundle channel. The most differential pressures in the axial and transverse direction on the duct were measured, and a relatively three-dimensional pressure measurements have been done. Applicability of the RANS models and pressure drop in edge subchannels were investigated through experiments and simulations. The following conclusions were drawn:

(1) The RANS turbulence models could accurately characterize the pressure distribution in the wire-wrapped fuel bundle channel, and the smallest deviation between the experimental data and numerical results was observed for the SST k-ω model.
(2) The pressure periodicity in the axial and transverse directions, 1.0H (not 0.5H) was studied. The static pressure fluctuated and decreased periodically as the z-axis coordinate increased. The transverse differential pressure between two pressure taps in 180°
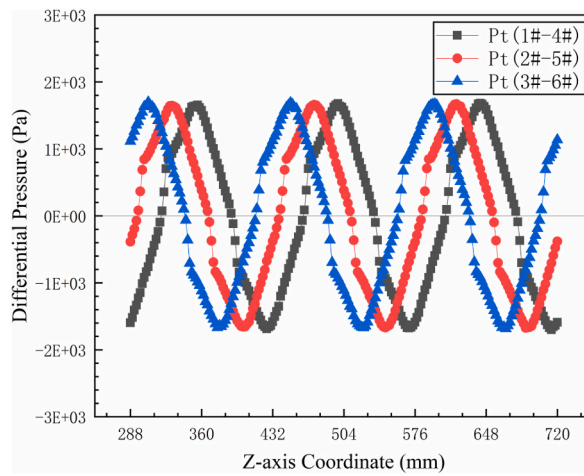
Fig. 11. Variation in transverse differential pressure with the z-axis coordinate between 2.0H and 5.0H when the Reynolds number was 15,000.
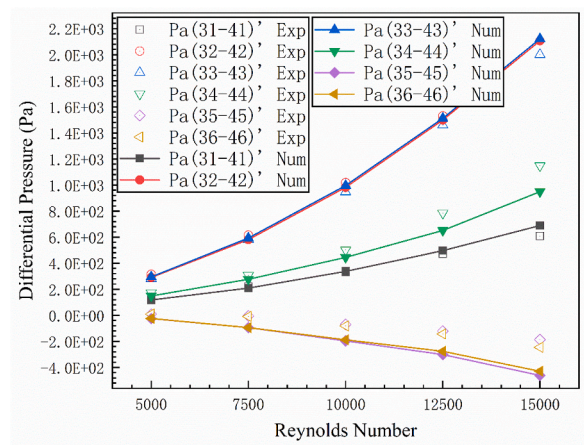

Fig. 12. Comparison between the experimental data and numerical results of axial differential pressure in 0.5H.
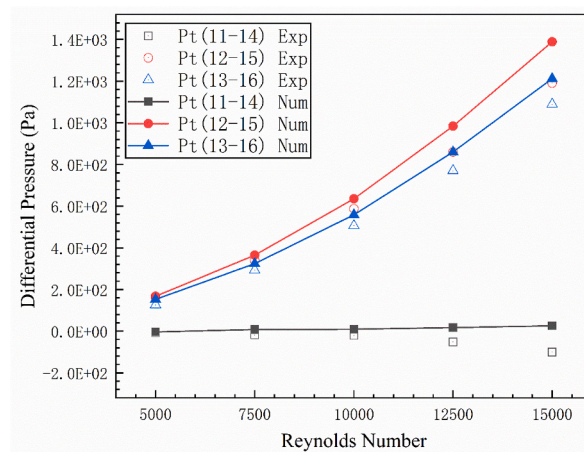

Fig. 13. Comparison between the experimental data and numerical results of transverse differential pressure at 1R
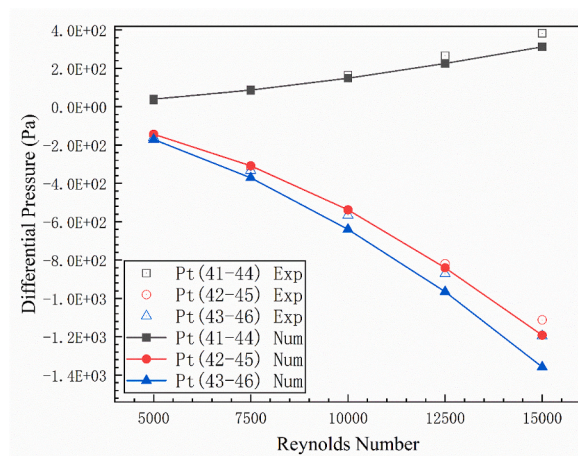
Fig. 14. Comparison between the experimental data and numerical results of transverse differential pressure at 4R
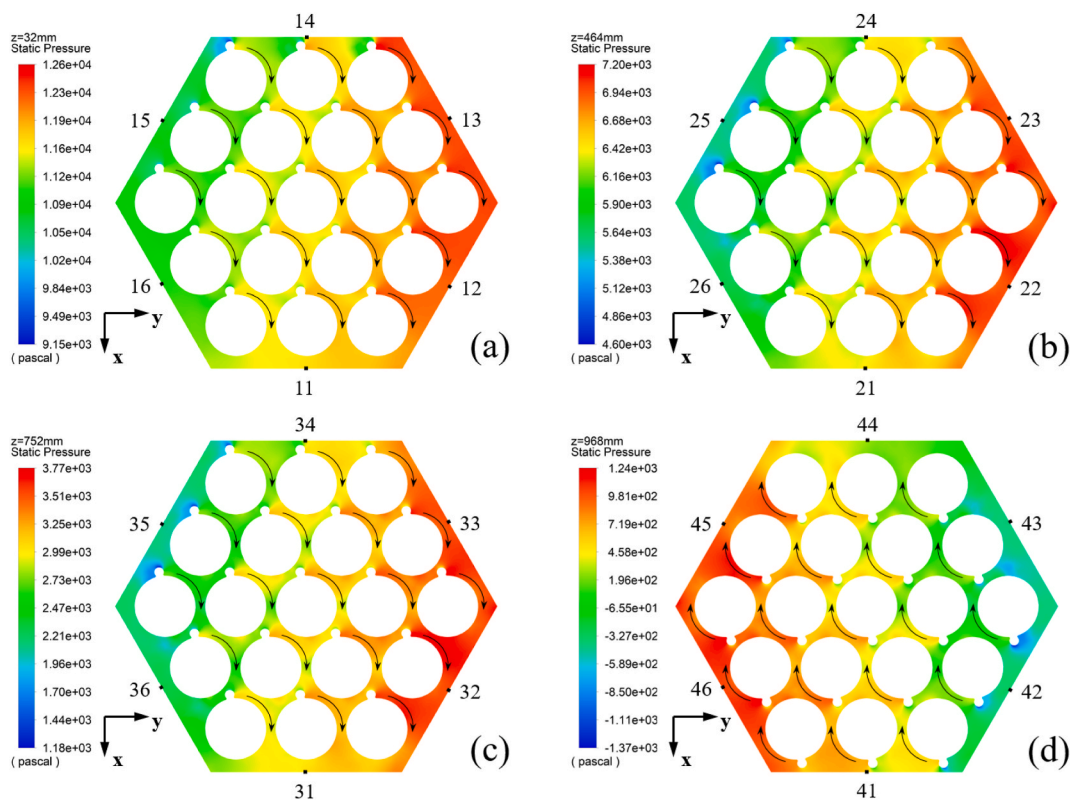

Fig. 15. Pressure contours at the four cross sections: (a) cross section at 1R; (b) cross section at 2R; (c) cross section at 3R; (d) cross section at 4R

direction in the edge subchannels varied periodically with the z-axis coordinate. The variation was similar to the sine function, and the variation period was 1.0H. Except for the minor fluctuation close to the wire-wrapped spacers, the phase difference between two adjacent curves was 1/6 H. The ratio of the maximum transverse differential pressure (~1670 Pa) to the average axial pressure drop within 1.0H (~1756 Pa) was approximately 95%. Moreover, as the axial height increased by 1/6 H, the pressure distribution contours rotated by 60° in the clockwise direction and the pressure values fluctuated and decreased.

(3) The differences between the experimental data and numerical results of the axial differential pressure were smaller than those of the transverse differential pressure. This was because the transverse differential pressures were smaller than the axial differential pressures and the pressure gradients close to the wire-wrap spacers were larger. Thus, it was challenging to accurately measure the transverse differential pressures, particularly at locations close to the wire-wrap spacers.
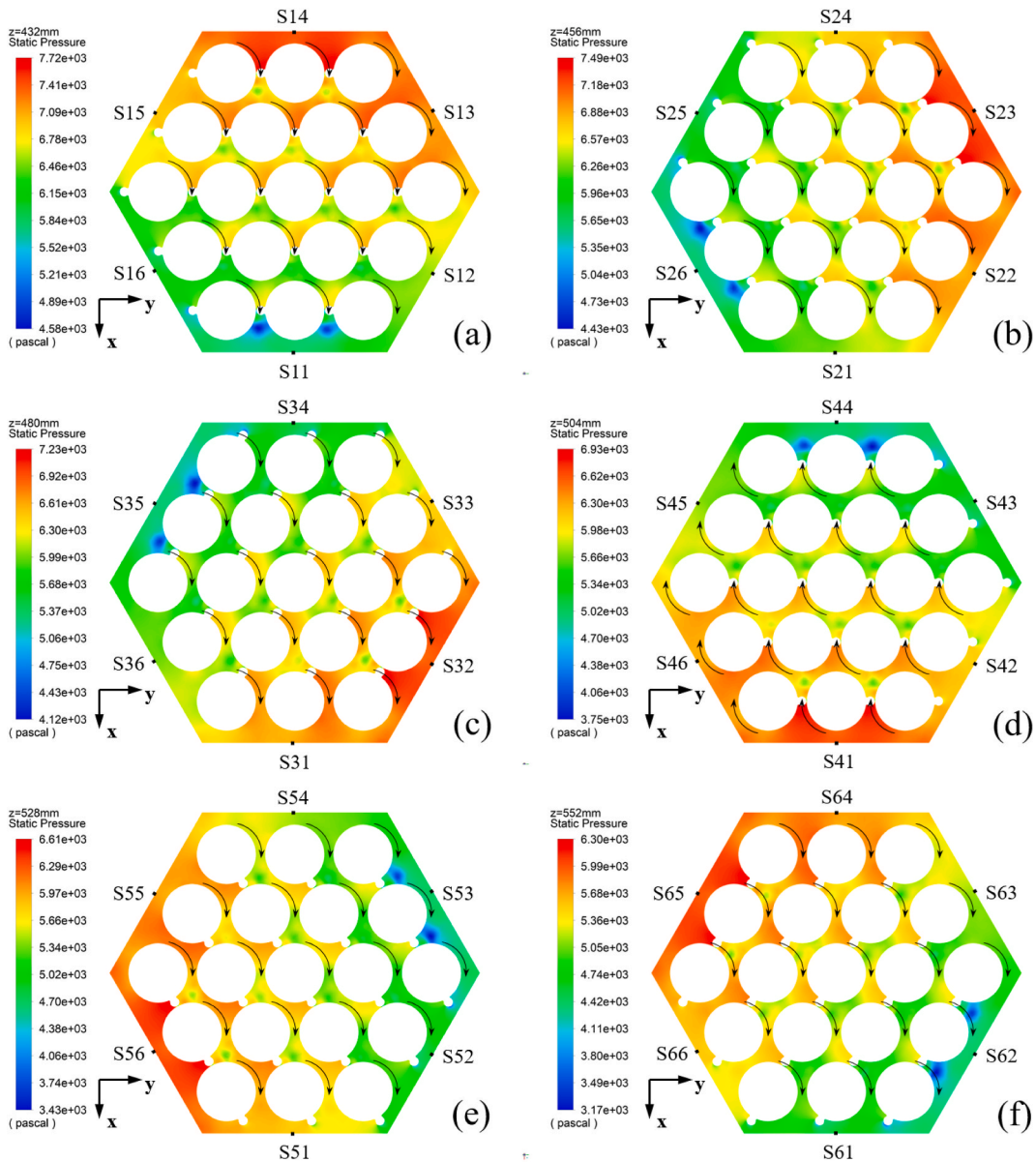
Fig. 16. Pressure contours at different cross sections from 3.0H to 3.0 and 5/6 H at intervals of 1/6 H: (a) 3.0H; (b) 3.0 and 1/6 H; (c) 3.0 and 1/3 H; (d) 3.0 and 1/2 H; (e) 3.0 and 2/3 H; (f) 3.0 and 5/6 H.

(4) The wire-wrapping structure enhanced the mixing of the working fluid. There were evident high-pressure and low-pressure areas in the transverse direction, the high-pressure areas appear at about 90° forward of the wire-wrap spacers' rotation direction, and large pressure gradients can be seen close to wire-wrap spacers. Along the forward the wire-wrap spacers' direction, the pressure downstream of the wire-wrap spacers was larger than that upstream of the wire-wrap spacers.

In this study, all the pressure taps were located in the edge subchannels. In future studies, pressure taps could also be placed in the inner and corner subchannels. In addition, the velocity distribution and cross-flow characteristics in a 19-pin fuel bundle channel at different Reynolds numbers are investigated by the Particle Image Velocimetry, and a refractive index matching solution of 62.932 wt % sodium iodide-36.968 wt% deionized water-0.1 wt% sodium thiosulfate is being prepared.

Funding

Accelerator Driven System (2017-000052-75-01-000590).

Author contribution statement

Data availability statement

Data included in article/supplementary material/referenced in article.

Declaration of competing interest

The authors declare that they have no known competing financial interests or personal relationships that could have appeared to influence the work reported in this paper

Acknowledgments

Nomenclature

CFD	computational fluid dynamics
CiADS	China initiative accelerator-driven system
H/D	lead-pitch-to-rod diameter ratio
LBE	lead or lead-bismuth eutectic
LES	Large eddy simulation
LFR	lead-cooled fast reactor
P/D	pitch-to-rod diameter ratio
PIV	Particle Image Velocimetry
RANS	Reynolds-averaged Navier–Stokes
Re	Reynolds number
RMS	root-mean-square
RSM	Reynolds Stress Model
SIMPLE	Semi-Implicit Method for Pressure Linked Equations
SP	starting point
SST	shear stress transport
UCTD	Upgraded Chen and Todreas Detailed
VHELP	Visual Hydraulic ExperimentaL Platform

References

[1] W.L. Zhan, H.S. Xu, Advanced Fission Energy Program - ADS transmutation system, Bull. Chin. Acad. Sci. 27 (3) (2012) 375–381.
[2] L. Gu, X.L. Su, Latest research progress for LBE coolant reactor of China initiative accelerator driven system project, Front. Energy 15 (4) (2021) 22.
[3] R. Yu, L. Gu, X. Sheng, et al., Review of fuel assembly design in lead-based fast reactors and research progress in fuel assembly of China initiative accelerator driven system, Int. J. Energy Res. 45 (8) (2021) 11552–11563.
[4] C. Schroer, et al., Corrosion kinetics of Steel T91 in flowing oxygen-containing lead–bismuth eutectic at 450 C, J. Nucl. Mater. 431 (1–3) (2012) 105–112.
[5] J. Ejenstam, P. Szakalos, Long term corrosion resistance of alumina forming austenitic stainless steels in liquid lead, J. Nucl. Mater. 461 (2015) 164–170.
[6] L.I. Sedov, Similarity and Dimensional Methods in Mechanics, tenth ed., CRC Press, Boca Raton, 1993.
[7] D. Fan, et al., Review of refractive index-matching techniques of polymethyl methacrylate in flow field visualization experiments, Int. J. Energy Res. 2023 (2023), 3413380.
[8] G. Su, H. Gu, X. Cheng, Experimental and numerical studies on free surface flow of windowless target, Ann. Nucl. Energy 43 (2012) 142–149.
[9] G.K. Batchelor, The application of the similarity theory of turbulence to atmospheric diffusion, Q. J. R. Meteorol. Soc. 76 (328) (1950) 133–146.
[10] R. Vaghetto, et al., Pressure measurements in a wire-wrapped 61-pin hexagonal fuel bundle, J. Fluid Eng. 140 (3) (2017).
[11] S.K. Chen, N.E. Todreas, N.T. Nguyen, Evaluation of existing correlations for the prediction of pressure drop in wire-wrapped hexagonal array pin bundles, Nucl. Eng. Des. 267 (2014) 109–131.

[12] Y. Liang, et al., An experiment study of pressure drop and flow distribution in subchannels of a 37-pin wire-wrapped rod bundle, Appl. Therm. Eng. 174 (2020) 13.

[13] G. Padmakumar, et al., Hydraulic characteristics of a fast reactor fuel subassembly: an experimental investigation, Ann. Nucl. Energy 102 (2017) 255–267.

[14] Y.S. Jeong, J.Y. Kim, I.C. Bang, Enhanced heat transfer and reduced pressure loss with U-pattern of helical wire spacer arrangement for liquid metal cooled-fast reactor fuel assembly, Ann. Nucl. Energy 135 (2020).

[15] M. Childs, et al., Experimental determination and analysis of the transverse pressure difference in a wire-wrapped rod bundle, Int. J. Heat Mass Tran. (2021) 170.

[16] C. Menezes, R. Vaghetto, Y.A. Hassan, Experimental investigation of the subchannel axial pressure drop and hydraulic characteristics of a 61-pin wire wrapped rod bundle, J. Fluid Eng.: Trans. ASME (5) (2022) 144.

[17] T. Nguyen, et al., Stereoscopic PIV measurements of near-wall flow in a tightly packed rod bundle with wire spacers, Exp. Therm. Fluid Sci. 92 (2018) 420–435.

[18] N. Goth, et al., PTV/PIV measurements of turbulent flows in interior subchannels of a 61-pin wire-wrapped hexagonal fuel bundle, Int. J. Heat Fluid Flow 71 (2018) 295–304.

[19] H. Kim, et al., Investigations of single-phase flow mixing characteristics in a wire-wrapped 37-pin bundle for a sodium-cooled fast reactor, Ann. Nucl. Energy 87 (2016) 541–546.

[20] J.H. Jeong, M.S. Song, K.L. Lee, CFD investigation of three-dimensional flow phenomena in a JAEA 127-pin wire-wrapped fuel assembly, Nucl. Eng. Des. 323 (2017) 166–184.

[21] L. Liu, S. Wang, B. Bai, Thermal-hydraulic comparisons of 19-pin rod bundles with four circular and trapezoid shaped wire wraps, Nucl. Eng. Des. 318 (2017) 213–230.

[22] E. Merzari, et al., Benchmark exercise for fluid flow simulations in a liquid metal fast reactor fuel assembly, Nucl. Eng. Des. 298 (2016) 218–228.

[23] D. Dovizio, A. Shams, F. Roelofs, Numerical prediction of flow and heat transfer in an infinite wire-wrapped fuel assembly, Nucl. Eng. Des. 349 (2019) 193–205.

[24] D. Dovizio, et al., Validating RANS to predict the flow behavior in wire-wrapped fuel assemblies, Nucl. Eng. Des. 356 (2020).

[25] O. Bovati, et al., RANS simulations for transition and turbulent flow regimes in wire-wrapped rod bundles, Int. J. Heat Fluid Flow 90 (2021).

[26] O. Bovati, et al., Pressure drop and flow characteristics in partially blocked wire wrapped rod bundles, Ann. Nucl. Energy 165 (2022) 13.

[27] M. Childs, et al., Experimental study on the effect of localized blockages on the friction factor of a 61-pin wire-wrapped bundle, J. Fluid Eng. 142 (11) (2020).

[28] Y. Wu, et al., Subchannel thermal-hydraulic analysis of the fuel assembly for liquid sodium cooled fast reactor, Prog. Nucl. Energy 68 (2013) 65–78.

[29] S. Pramuditya, M. Takahashi, Thermal–hydraulic analysis of wire-wrapped SFR test subassemblies by subchannel analysis method, Ann. Nucl. Energy 54 (2013) 109–119.

[30] D.J. Fan, et al., Periodicity and transversal pressure distribution in a Wire-wrapped 19-Pinfuel assembly, Int. J. Energy Res. (3) (2020).

[31] R. Li, et al., PIV and CFD study on crossflow characteristics in a 7-pin wire-wrapped bundle channel, Int. J. Energy Res. 2023 (2023), 5542001.

[32] F. Roelofs, et al., Review of fuel assembly and pool thermal hydraulics for fast reactors, Nucl. Eng. Des. 265 (2013) 1205–1222.

[33] W.D. Pointer, et al., RANS-Based CFD Simulations of Sodium Fast Reactor Wire-Wrapped Pin Bundles, 2009.

[34] E. Merzari, et al., Numerical simulation of the flow in wire-wrapped pin bundles: effect of pin-wire contact modeling, Nucl. Eng. Des. 253 (2012) 374–386.

[35] A. Ahmad, K.-Y. Kim, Three-dimensional analysis of flow and heat transfer in a wire-wrapped fuel assembly, in: Proc. of ICAPP, 2005.

[36] T. Sreenivasulu, B. Prasad, Flow and heat transfer characteristics in a seven tube-bundle wrapped with helical wires, Int. J. Adv. Technol. 2 (3) (2011) 350–381.

[37] P. Zhao, et al., CFD analysis of transverse flow in a wire-wrapped hexagonal seven-pin bundle, Nucl. Eng. Des. 317 (2017) 146–157.

[38] K. Rehme, Pressure drop correlations for fuel element spacers, Nucl. Technol. 17 (1) (1973) 15–23.

[39] S.-K. Cheng, N.E. Todreas, Hydrodynamic models and correlations for bare and wire-wrapped hexagonal rod bundles — bundle friction factors, subchannel friction factors and mixing parameters, Nucl. Eng. Des. 92 (2) (1986) 227–251.

[40] E. Novendstern, Turbulent flow pressure drop model for fuel rod assemblies utilizing a helical wire-wrap spacer system, Nucl. Eng. Des. 22 (1) (1972) 28–42.

[41] F. Engel, R. Markley, A. Bishop, Laminar, transition, and turbulent parallel flow pressure drop across wire-wrap-spaced rod bundles, Nucl. Sci. Eng. 69 (2) (1979) 290–296.

[42] A. Zhukov, et al., Analysis of friction factor in the bundle fast reactor fuel subassembly, Atom. Energy 60 (1986) 317–321.

[43] U. Bieder, H. Uitslag-Doolaard, B. Miku, Investigation of pressure loss and velocity distribution in fuel assemblies with wire-wrapped rods by using RANS and LES with wall functions, Ann. Nucl. Energy (2020).

[44] J.-H. Jeong, M.-S. Song, K.-L. Lee, RANS based CFD methodology for a real scale 217-pin wire-wrapped fuel assembly of KAERI PGSFR, Nucl. Eng. Des. 313 (2017) 470–485.